Microscopy and Microanalysis (2020), **26**, 112–119
doi:10.1017/S1431927619015319

Microscopy AND Microanalysis

Original Article

Depth Profile Analysis of Thin Oxide Layers on Polycrystalline Fe–Cr

Gerrit Zijlstra[1], Tomáš Šamořil[2], Hana Tesařová[2], Václav Ocelík[1]* and Jeff Th. M. De Hosson[1]

[1]Department of Applied Physics, Materials Innovation Institute and Zernike Institute for Advanced Materials, University of Groningen, Nijenborgh 4, 9747 AG Groningen, the Netherlands and [2]TESCAN ORSAY HOLDING, a.s., Libušina tř. 21, 623 00 Brno, Czech Republic

Abstract

Surfaces of polycrystalline ferritic Fe–Cr steel with grain sizes of about 13 μm in diameter were investigated with surface sensitive techniques. Thin oxide layers, with a maximum thickness of about 100 nm, were grown by oxidation in air at temperatures up to 450°C and were subsequently characterized using time-of-flight secondary ion mass spectrometry (TOF-SIMS) and atomic force microscopy. Correlative microscopy was applied, which allows for element-specific depth profiles on selected grains with a particular crystal orientation. A strong correlation between the grain orientation and the thickness of the oxide layer was found. The sequence in the oxidation growth rate of ferritic Fe–Cr steel crystal planes is found to be {011} > {111} > {001}, which is unexpectedly opposed to known Fe-based systems. Moreover, for the first time, the Cr/Fe ratio throughout the oxide layer has been determined per grain orientation. A clear order from high to low of {001} > {111} > {011} was detected.

Key words: corrosion, EBSD, polycrystalline, Fe-Cr steel, TOF-SIMS

(Received 12 February 2019; revised 25 October 2019; accepted 19 December 2019)

Introduction

Stainless steel develops a passive layer which protects the bulk from further corrosion. The resulting passive layer is between 2 and 10 nm thin (Cabrera & Mott, 1949). In general, for stainless steel, the structure and chemical composition of this layer depend on the conditions present at formation, e.g. dry and wet chloride-containing environments or acidic solutions, for which the thickness can vary in the range from 1 to 4 nm (Jin & Atrens, 1990). For an overview of the growth of ultrathin passive films, reference is made to Maurice & Marcus (2012).

Upon heating, the equilibrium of the passive film is disrupted. The passive film thickens until a thermal oxide layer is formed, which acts as a barrier for further corrosion. The formation of oxides has been studied extensively in iron, as it is a base metal in many (structural) alloys. The oxidation of iron is very well described by Vernon et al. (1939, 1953). When bcc iron is heated above 200°C in air, a duplex oxide layer will form. The inner oxide consists of Fe_3O_4, also known as magnetite, the outer of Fe_2O_3 (hematite). For an extensive background on iron oxides as Fe_2O_3 and Fe_3O_4, the reader is referred to Weiss & Ranke (2002) and Parkinson (2016).

The protective passive layer on ferritic Fe–Cr steel consists of a mixed film of iron- and chromium oxides such as $(Fe,Cr)_2O_3$ and $(Fe,Cr)_3O_4$ (Olsson & Landolt, 2003), with a thickness of the order of several nanometers (Olefjord & Fischmeister, 1975; Jin & Atrens, 1990; Ramachandran et al., 2016). At high temperatures, the thickness of this layer can reach the sub-millimeter range, as seen on steel exposed to steam at 600°C (Pujilaksono et al., 2011; Jonsson et al., 2013, 2016), 700°C (Yuan et al., 2016), and 1,000°C (Saeki et al., 1998).

Apart from the conventional techniques, recently, time-of-flight secondary ion mass spectrometry (TOF-SIMS) has also been used to examine the oxide layer on steel, for example to characterize the oxide layer on 316 L (Tardio et al., 2015), the micrometer thick oxide layer on 310 SS (Grinberg Dana et al., 2014), coated steel (Díaz et al., 2014), and the oxide layer on 304 L after exposure of steam (Mamede et al., 2016). These studies focused on the general chemical composition of the oxide layer. TOF-SIMS has been used for more localized phenomena, such as pitting on CrNi steel (Rossi et al., 2000) or steel under bacterial attack (Seyeux et al., 2015).

The particular oxide growth and composition along the three main directions, i.e. ⟨100⟩, ⟨110⟩, and ⟨111⟩, are studied on, e.g. bcc iron (Qin et al., 2003; Ossowski & Kiejna, 2015), chromium (Ekelund & Leygraf, 1973; Michel & Jardin, 1973; Gewinner et al., 1978; Maurice et al., 2000), or Fe–Cr (Lince et al., 1992; Fujiyoshi et al., 2012) single crystals. Only a single study focused on the orientation of oxides found on polycrystalline Fe–Cr steel, with respect to the substrate (Kim et al., 2011). Due to the high temperatures (650–800°C) and a Cr content of 22%, mainly Cr oxides were found. To this end, we recently added a study on Fe–Cr steel with 13% Cr, oxidized up to a temperature of 450°C (Zijlstra et al., 2018). Here, a mixture of iron- and chromium-containing oxides was found. The observed sequence in the oxidation rate of crystal planes parallel to the surface for Fe–Cr steel was {001} < {111} and {011}.

Despite this work, the local chemical composition is unknown and characterization of thin oxide layers on a polycrystalline material remains a challenge. In this work, we try to push this length-scale downwards to polycrystalline steel with grains of

***Author for correspondence:** Václav Ocelík, E-mail: v.ocelik@rug.nl

Cite this article: Zijlstra G, Šamořil T, Tesařová H, Ocelík V, De Hosson JThM (2020) Depth Profile Analysis of Thin Oxide Layers on Polycrystalline Fe–Cr. *Microsc Microanal* **26**, 112–119. doi:10.1017/S1431927619015319

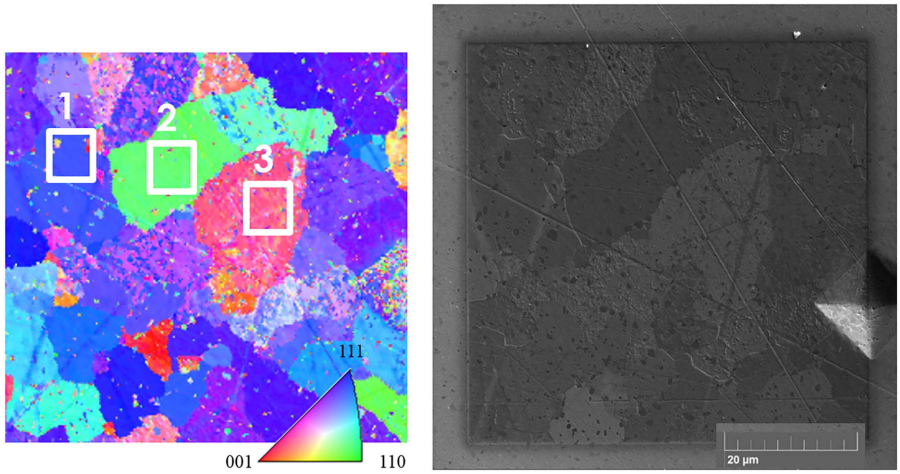

Fig. 1. Left: [001] Inverse Pole Figure map. Areas 1, 2, and 3 are located within grains with ⟨111⟩, ⟨011⟩, and ⟨001⟩ directions normal to the sample surface, respectively. **Right:** SEM image of the same area after TOF-SIMS mapping.

only 10 μm or less in diameter. The chemical composition of thermal grown oxide layers (100 nm and thinner) will be determined on grains along the three main crystallographic directions, i.e. ⟨100⟩, ⟨110⟩, and ⟨111⟩.

Method and Materials

The material under investigation is an Fe–Cr alloy with 13 wt% Cr of class AISI 420 (minimum 0.15 wt% C; maximum 1 wt% Si, 1 wt% Mn, 0.04 wt% P, and 0.030 wt% S). The microstructure consists of ferritic grains of about 13 μm in size and chromium carbides of about 1 μm. Specimens were cut from a strip of this stainless steel and mirror polished, where the final step included polishing with 0.25 μm diamond particles. A colloidal water-based silica particle suspension was not used to avoid chemical etching. Exposure to water was also prevented by making use of an alcohol-based lubricant during polishing with diamond particles. After polishing, the specimens were rinsed with ethanol and dried in hot air. Recovery of the passive layer was executed in ambient conditions, i.e. at room temperature and 50% relative humidity (RH), for at least 24 h.

The corrosion films were established by oxidizing the mirror polished and recovered surfaces in air. The specimens were put in a quartz tube with openings at both ends and were introduced into a heat induction furnace. The temperature was measured with a thermocouple placed inside the quartz tube and kept constant within ±5°C. The applied temperatures are typically used at annealing for stress relief and well above the 200°C to stimulate Fe diffusion to the surface (Vernon et al., 1953). Specimens kept at 300°C for 20 min resulted in the yellow-gold surface. Those brought to 450°C with a dwell time of 20 min established a blueish surface.

Prior to oxidation, micro-indents had been made as reference markers. The surface was indexed with electron backscatter diffraction (EBSD) using a Philips XL30 ESEM (Phillips, Eindhoven, the Netherlands) scanning electron microscope with an EDAX EBSD Digiview 3 detector (EDAX Inc., Draper, UT, USA) operated at 20 kV acceleration voltage and using a probe current of the order of 1 nA. Suitable grains were selected with the distinct crystal orientations close to {111}, {011}, and {001} planes parallel to the sample surface, respectively. The average grain diameter ranges between 10 and 15 μm. An area of 60 × 60 μm^2 containing the selected grains was profiled with TOF-SIMS, using a LYRA3 focused ion beam scanning electron microscope (FIB-SEM) system (TESCAN, Brno, Czech Republic) with a C-TOF module provided by TOFWERK (Thun, Switzerland). The FIB gun of the FIB-SEM was operated in a raster over the selected area. The primary ion beam for sputtering consists of gallium ions having energy of 10 keV and a total current of 200 pA. In this configuration, a spot size and thus a lateral resolution of about 80 nm in diameter were attained. The spots were binned (4 × 4) in an image (frame) of 1,024 × 1,024 pixels. From the stack of frames, a 3D sampling is obtained. From this data, one can select an area on the surface and extract the counts of the selected ion throughout the frames. The marker indents and the appearance of the microstructure after grain-orientation mapping assisted the location of the area of interest. An example of a region with defined areas is shown in Figure 1.

Results and Discussion

Purple Oxidized Surface

A thin oxide film was established by heating a mirror polished specimen in air at 450°C for 20 min, resulting in a characteristic purple–blue-ish surface. The surface color provides an indication of the thickness of the oxide. For temper colors, the order from thinner to thicker oxide layers is straw yellow, brown yellow, rosy mauve, and blue (Evans, 1925). For iron, an oxide thickness of 35 nm (straw yellow) and 59 nm (blue) has been reported by Vernon et al. (1939), and 46 and 72 nm for straw and blue by Constable (1928). In this work, we assume the oxide layer of the purple surface being less than 100 nm.

Two areas of 60 × 60 μm^2 were mapped with TOF-SIMS operating in the positive mode and the negative mode for the two respective areas. The cross-sections of this sampling are shown for the ions O^-, Cr^+, CrO_2^-, Fe^+, and FeO_2^-, as depicted in Figure 2. The surface contains an oxygen-rich layer, which is divided into two sublayers with an enrichment of FeO_2^- at the top and CrO_2^- at the bottom. The secondary ions FeO_2^- and CrO_2^- are characteristic for the oxide species present in the film. In an earlier work with X-ray photoelectron spectroscopy and grazing incidence X-ray and neutron diffraction on this type of steel, the presence of this dual layer has also be shown to be an

https://doi.org/10.1017/S1431927619015319 Published online by Cambridge University Press

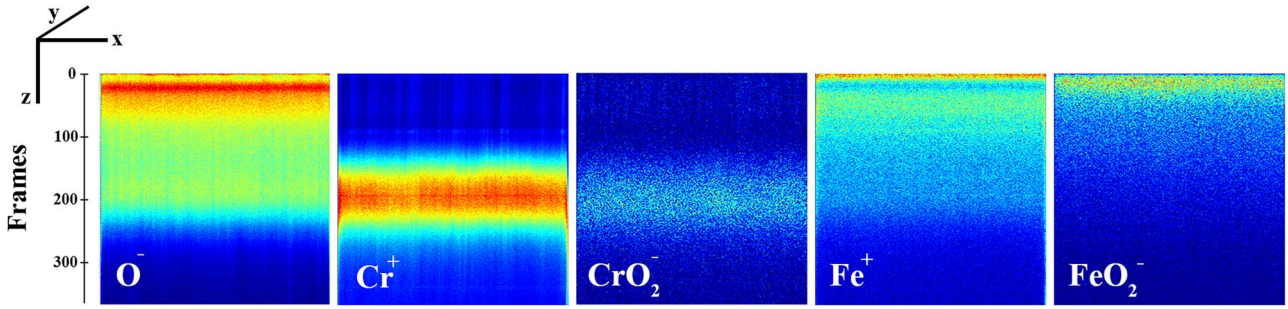

Fig. 2. Cross section of stacked frames obtained by TOF-SIMS, for the ions O^-, Cr^+, CrO_2^-, Fe^+, and FeO_2^-. The *x*-axis (frontal) and the *y*-axis (perpendicular to the plane, integrated signal) are both 60 μm; the *z*-axis (top to bottom) is constructed by the frames, with frame 0 at the top as the initial outer surface. The color code represents the count intensity, with red as the highest intensity and blue as the lowest with zero counts. The maximum (red) is different for each image.

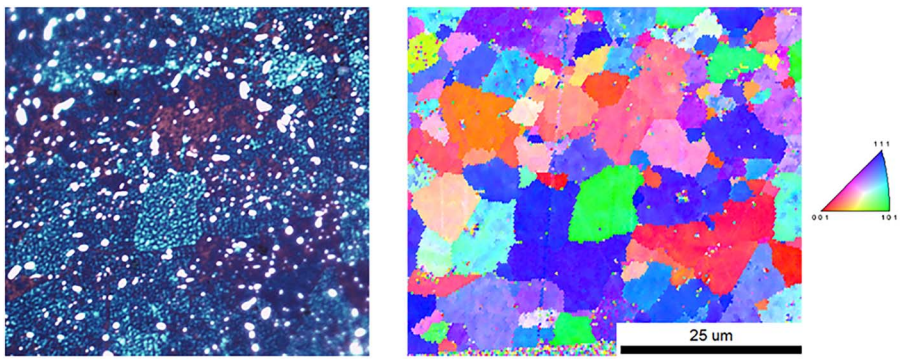

Fig. 3. Left: optical image of the purple oxidized surface. **Right:** [001] IPF map of the same area as in the optical image.

iron oxide (Fe_2O_3)-rich surface layer, with an inner Fe_3O_4 layer, which also has a chromium enrichment (Zijlstra et al., 2018). Thin vertical lines can be seen on the Cr^+ cross section. These lines originate from the chromium carbides. Their contributions to the overall Cr^+ count are relatively small. The curtaining in the Fe^+ and FeO_2^- images is also attributed to the presence of chromium carbides, as they cause a local depletion (dark lines in the images) of iron (oxides).

An optical image of a typical area is shown in Figure 3, together with the [001] Inverse Pole Figure (IPF) map of the bulk grains at the surface.

The shape of the grain in the center with {011} crystal planes parallel to the surface (color code green in Fig. 3, right) is also clearly seen in the optical image as a bright light blue area. The red color-coded grains with the orientation toward the ⟨001⟩ direction are recognized in the optical image as dark red–purple areas; in particular, seen above the center ({101} oriented-) grain, as well as on the bottom right-side. The colors observed with the optical microscope can be placed in an oxidation thickness color palette. The bright blue indicates a thicker oxide layer than the dark red areas (Evans, 1925).

Two grains of each of the three principal orientations {111}, {011}, and {001} were selected, from which the O^- depth profile was extracted. The oxygen depth profiles of these six grains are plotted in Figure 4. Frame 0 is the frame obtained from the surface. A higher frame number indicates a measurement from deeper into the surface. From the plot, it is seen that the amount of detected oxygen shows a spike at the surface. This can be due to the presence of, e.g., organic (carbonaceous) contaminants at the surface. The spike and the drop of the first few recorded frames are considered as artifacts. After about 200 frames, the amount of oxygen counts starts to decrease significantly, which can be correlated to the approach of the end of the oxide layer. The oxide signal is almost zero at 300 frames, marking the end of the oxide layer. However, there is a difference between the lines originating from the oxides on the different bulk grain orientations. The oxygen count for the grains with the ⟨001⟩ direction goes first toward zero, then the {111} oriented grain, followed by the {011} grain as the last one. This indicates that the oxide thickness is not equal on each grain; in fact for this specimen, it depends on the grain orientation in the order of {011} > {111} > {001}.

A similar area of $60 \times 60\ \mu m^2$ was mapped in the so-called positive mode. Here also, three main grain orientations were selected, from which both the Fe^+ and Cr^+ depth profiles were extracted. The counts of both ions from each frame have been divided in order to obtain the measured Cr^+/Fe^+ ratio throughout the oxide layer for each crystal orientation. These Cr^+/Fe^+ ratio profiles are shown in Figure 5. The outer layer of the surface consists of mainly iron oxide, resulting in a ratio of almost zero for 125 frames. Thereafter, the enrichment zone of chromium is reached, giving a notable increase in the ratio. This increase, however, is different for the three distinct grain crystal orientations. Clearly, the grains with the {001} plane parallel to the surface have the highest ratio peaking at $Cr^+/Fe^+ = 3.5$, followed by the {111} plane ($Cr^+/Fe^+ = 2$) and then the {110} plane ($Cr^+/Fe^+ = 1.5$).

The Cr/Fe ratio is an important parameter for the corrosion resistance of the passive or oxide layer, where a higher Cr content indicates a better corrosion resistance. There are multiple phases, such as Fe_2O, Fe_3O_4, chromium oxides, chromium carbides, and the Fe–Cr bulk matrix. The type of the ion (cluster) generated by the primary ion beam depends on the local chemical composition. It has to be noted that the calculated ratio here does not

https://doi.org/10.1017/S1431927619015319 Published online by Cambridge University Press

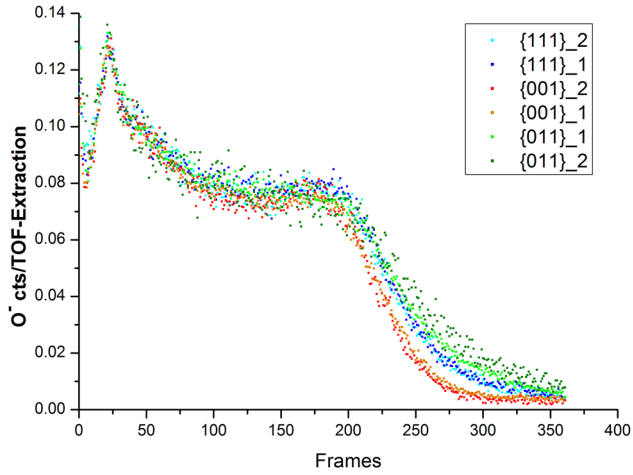

Fig. 4. Depth profile for O^- of two grains (six in total) of each of the three main crystal orientations after a thermal treatment at 450°C in air. The *y*-axis shows the ratio of oxygen counts/TOF extraction, which is given by the number of oxygen counts per frame divided by the number of pixels of the selected area (grain).

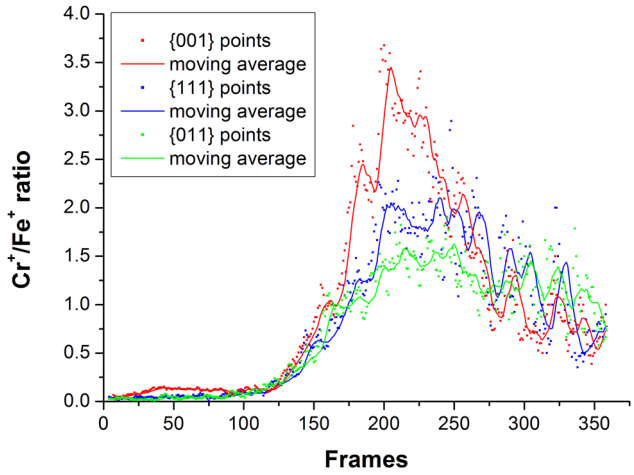

Fig. 5. Cr^+/Fe^+ ratio throughout the oxide layer for the three main crystal orientations after a thermal treatment at 450°C in air. The data points are obtained by applying a moving average of six frames for the counts of Cr^+ and Fe^+, respectively, before calculation of the ratio. The solid lines are an average of this ratio constructed from points in the graph, applying a moving average of 10 for the three series.

represent the atomic ratio (distribution), as the relative sensitivity of each element is inversely proportional to the sputtering yield. The yield for Cr^+ is lower than that for Fe^+. For more details, the reader is referred to Giannuzzi & Stevie (2005).

The ratio for the FeO_2^- and CrO_2^- ions, characteristic for the oxide species, has been determined in a similar way as for the Cr^+/Fe^+ ratio; however, the profiles have been extracted from an area mapped in the negative mode and are shown in Figure 6.

Yellow Oxidized Surface

A different specimen was heated in air at 300°C for 20 min, resulting in a typical gold/yellow surface. The O^- profile is shown in Figure 7a. After about 70 frames, the amount of counts starts to reduce significantly. As with the purple oxidized surface, there is also a difference between the profiles originating from the oxides on the different bulk grain orientations. Both profiles on {001} and {011} grains reach their oxide minimum earlier compared to profile on the {111} grain. The oxygen profiles of the ⟨001⟩ and ⟨011⟩ direction grains are almost equal. From these oxide depth, profiles can therefore be deduced that the oxidation for the yellow oxidized specimen progresses in the order {111} > {011} and {001}, which is different from the thicker oxide on the purple surface with the order {011} > {111} > {001}.

The Cr^+/Fe^+ ratio in Figure 7c shows identical curves for {001} and {011} grain orientations. Although the ratio of the {111} orientation seems to peak a little higher, the width is comparable to the other orientations. The differently oriented grains seem to have a similar Cr^+/Fe^+ ratio after this specific heat treatment.

Nonoxidized Reference Surface

The previous results are compared with a nonoxidized reference specimen. This surface was two times mirror polished, including a final step with ¼ micron particles with an alcohol-based lubricant to avoid etching and advanced corrosion due to excess water exposure. After polishing, the sample was kept at room temperature in an environment with air of 50% RH for 48 h to restore the passive layer. After the first polishing sequence, indents were made to serve as a reference point for an EBSD grain-orientation mapping. EBSD mapping requires the exposure of the surface to the electron beam

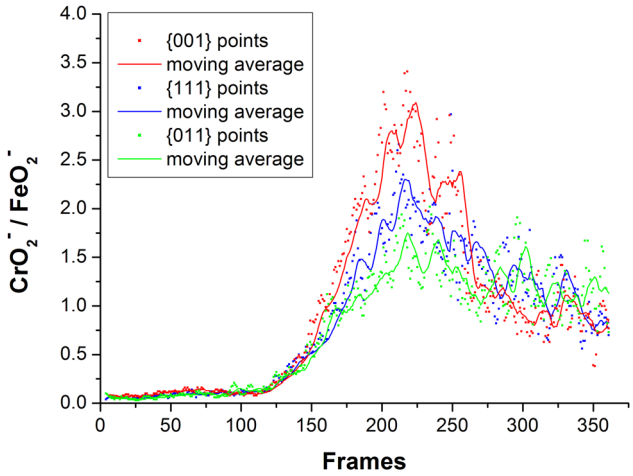

Fig. 6. CrO_2^-/FeO_2^- ratio throughout the oxide layer for the three main crystal orientations after a thermal treatment at 450°C in air. The data points are obtained by applying a moving average of six frames for the counts of CrO_2^- and FeO_2^-, respectively, before calculation of the ratio. The solid lines are an average of this ratio constructed from points in the graph, applying a moving average of five for the three series.

for several hours, during in which processes such as hydro-carbon deposition are active. The very last polishing and recovery steps were repeated to annul any effects which could influence the passive layer. The various grains were not clearly distinguishable in the optical and electron microscopes, compared to the color oxidized specimens. After TOF-SIMS mapping, the grain boundaries and also contrast differences between the grains could be seen. This visual information combined with the known distance from the reference markers made it possible to select areas in grains with the orientations of interest. The oxygen depth profile of this reference for three grain orientations is shown in Figure 7b. Both {001} and {011} orientations reach the oxygen minimum earlier compared to the {111} orientation. From this, we might conclude that the oxide layer is slightly thicker on the {111} oriented grains.

On this sample, the Cr^+/Fe^+ ratio of Figure 7d shows identical curves for {001} and {111} orientations. Although the ratio of

https://doi.org/10.1017/S1431927619015319 Published online by Cambridge University Press

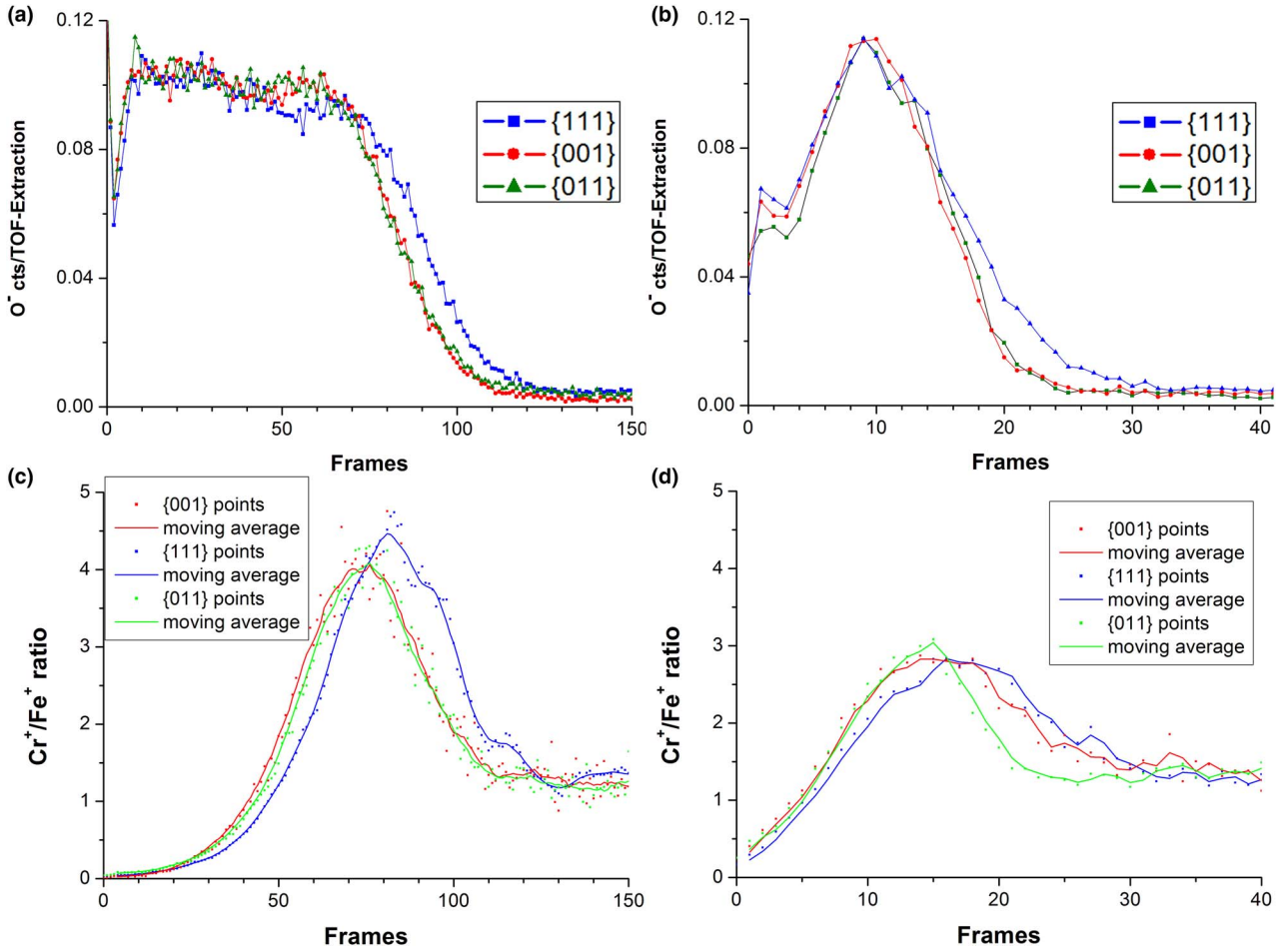

Fig. 7. Depth profile for O^- for grains of each of the three main crystal orientations. (**a**) After a thermal treatment at 300°C in air; (**b**) nonoxidized reference sample. The Cr^+/Fe^+ ratio throughout the oxide layer for the three main crystal orientations. (**c**) After a thermal treatment at 300°C in air; (**d**) the nonoxidized reference sample. The data points are obtained by applying a moving average of five frames for the counts of Cr^+ and Fe^+, respectively, before calculation of the ratio. The solid lines are an average of this ratio constructed from points in the graph, applying a moving average of five for the three series.

{011} seems to peak a little higher, the width of this peak is comparable to the other orientations. The different oriented grains seem to have a similar Cr^+/Fe^+ ratio after this specific heat treatment.

It is interesting to note that the peak of the chromium enrichment is at about the same depth, as where the oxygen content is decreasing for all three types of samples (see Figs. 4, 5, 7), so the chromium enrichment is always at the bottom of the oxide layer. It has been shown for air passivated stainless steel that the chromium enrichment is found as a layer just on top of the metallic bulk (Olefjord, 1975; Ramachandran et al., 2016). It appears that the diffusion of Cr cations slows down rapidly, once a thin layer of few nanometers of chromium (-type) oxide is formed.

The point where the oxygen signal is close to zero is reached after about 300 (purple), 100 (yellow), and 20 (nonoxidized) frames. When a rather conservative estimate of 5 nm for the thickness of the passive layer of the nonoxidized specimen is taken (Ramachandran et al., 2016), a thickness estimation can be made of 25 and 75 nm for the yellow (300°C) and purple (450°C) surface, respectively. It is tacitly assumed that the sputtering rate is not affected by the different orientations of ferritic grains in the substrate material when interpreting experimental results are shown in Figures 4 to 7. However, the whole situation seems to be more complicated. On one side, the oxidized surfaces may have different crystallographic characteristics than their corresponding "substrate" grains or they may be even amorphous. Therefore, the assumption that the crystallographic orientation of the substrate does not play an important role seems to be reasonable. On the other hand, the influence of all other factors on the sputtering rate (e.g. roughness, chemical composition, and bonding) is still a question. These effects, we believe, are partially suppressed by an approach where not only the sputtering profile of one element (oxygen) is plotted but also a combination (or ratio) of few of them is shown and discussed.

The generated TOF-SIMS depth profiles show that the thickness and the composition of the oxide layers differ, although they may give the impression that each grain has a uniform oxide layer from the lateral point of view. Therefore, the surface of the yellow oxidized specimen has been investigated with atomic force microscopy (AFM). The topography map is seen in Figure 8. The carbides with their typical size of ~0.5–1.0 μm are recognized by their slightly elongated shape. Their dark color code in the topography maps indicate that they are located deeper in the surface. It clearly shows that the carbide surface is flat, which is the result of the surface polish prior to oxidation. The rest of the matrix, however, is covered with round, spherical tips which are emerging from the matrix, creating a cauliflower-like surface. At the top, they possess a diameter of about 100 nm. It has to be

https://doi.org/10.1017/S1431927619015319 Published online by Cambridge University Press

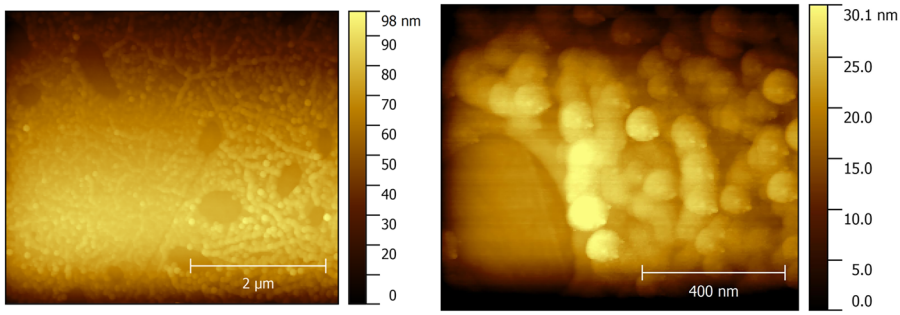

Fig. 8. AFM topography maps of a polished steel surface after heating at 300°C in air for 20 min. The lower areas (dark color code) with a diameter of about 0.5–1.0 μm are chromium carbides.

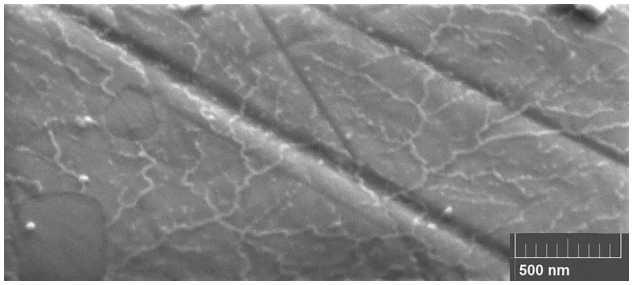

Fig. 9. SEM image of a polished steel surface after heating at 300°C in air for 20 min. Large diagonal grooves are left over scratches from sample polishing.

noted that the height differences between the tips are about 15 nm at maximum (as demonstrated at the side of the carbide in Fig. 8, right), where their lateral diameter is an order of magnitude higher. At this sub-micron scale, the surface is therefore best visualized as an undulating landscape. On Figure 8—left, traces of the spheres can be seen, forming a network sub-structure. This network structure is also pronounced in the SEM image taken from another part of the surface in the secondary electron mode, as shown in Figure 9. The cauliflower surface itself might be less pronounced in the SEM image due to the small height differences (which can be observed in sensitive AFM images), instead only the slightly bigger sub-structures are visible. These form a network of domains with lateral size in the order of 500 nm, much smaller than the average bulk grain size of 10–15 μm. Therefore, they cannot be related to microstructural features as grain boundaries. A detailed study of the nodular structures by combining SEM and AFM observations of the same area is a subject for the future work.

Also, the more advanced oxidized surface (450°C in air for 20 min) has been further investigated. An SEM close-up of this purple surface is shown in Figure 10. Similar to the mild oxidized specimen, spheres are found at the surface. Here, their size is about 400 nm in diameter, making them four times larger than the spheres of the specimen heated to 300°C in air. In order to determine the chemical composition of the spheres, the area was mapped with TOF-SIMS. The superimposed 3D map for Fe^+ (Fig. 10, top) shows a low intensity of Fe at the chromium carbides. The oxide spheres, however, match with high Fe intensities. The map of Figure 10, bottom also shows high oxygen concentrations at the spheres and low values for the carbides. On the other hand, the stacked frames for Cr show high Cr concentrations at the carbides, but low values for the oxide spheres. Chromium is also detected between the spheres. This chemical analysis makes clear that the carbides consist of mainly Cr with a small (thin) chromium oxide layer. Chromium oxides are known to be very stable where, for example, only a thin layer of a few nm of Cr_2O_3 gives sufficient protection against further thermal corrosion. The mainly Fe-rich matrix is more vulnerable to further oxidation. Although Cr enrichment is present at the oxide/bulk interface, the top part of the matrix oxide layer consists of mainly iron oxides, which tend to emerge in nodular structures. These structures lack in Cr; for the bigger spheres, the absence of chromium exists even further into the oxide.

The spheres or nodules have been observed previously (Higginson et al., 2015), but no relation to the grain orientation has been reported. However, in the work presented here, it has been observed that for the advanced (purple) oxidized specimen, the number of spheres is correlated to the grain orientation. For this surface, the {011} grains contained the most spheres, and the {001} grains the least. The distribution of spheres, therefore, follows the order {011} > {111} > {001}, similar to the thickness of the oxygen layer. The oxygen layer thickness and the Cr^+/Fe^+ ratio vary for grains of the three main crystal orientations, while the order can change with a different surface oxidation state. The spherical tips are actually a signature of the differences in chemical composition, as detected and displayed in Figures 4 to 6. The different oriented grains possess differences in the amount of chromium (oxide) enrichment. The lower chromium contents in the oxide layer offer inferior corrosion protection. On these grains, more iron oxides can be formed, which appear at the surface as nodules. This observation by AFM is a confirmation of the conclusions drawn based on the TOF-SIMS data: grains with a thicker iron oxide show more and larger nodules at the surface.

The orders are summarized in Table 1. Initially, for the non-oxidized reference and the yellow oxidized surface, the {111} orientation contains the thickest oxide layer to be exceeded by the {011} on the advanced purple oxidized surface. The {001} grains were found to have the thinnest oxide layer at this stage, but also the highest Cr^+/Fe^+ ratio.

A study on polycrystalline iron with grains of several hundreds of micrometers (heated for 1 h at 300°C in air) showed a clear distinction of the oxide thickness with respect to the crystal orientation (Takabatake et al., 2016). Although electrochemical tests on pure iron are not conclusive, the general rule that arises is that {001} planes are more susceptible for oxidation (Fushimi et al., 1999, 2013; Schreiber et al., 2007; Takabatake et al., 2016, 2017).

Whether the low Cr^+/Fe^+ ratio makes the {011} grains more susceptible to iron oxide sphere formation or vice versa, this grain orientation develops a thicker oxide than the {001} oriented grains. This outcome supports the conclusion made by Zijlstra

https://doi.org/10.1017/S1431927619015319 Published online by Cambridge University Press

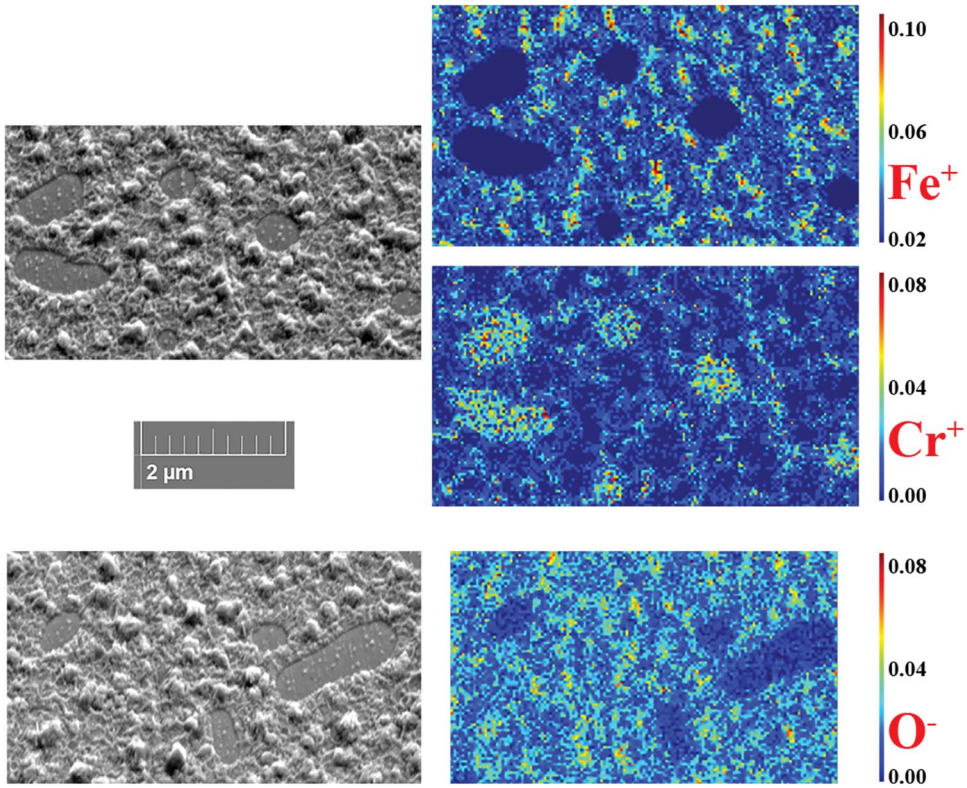

Fig. 10. Left column: SEM images of a polished steel surface after heating to 450°C in air for 20 min. Clearly visible are the flat carbides located deeper in the surface, and spheres decorating the surface. **Right column:** corresponding TOF-SIMS mappings of the SEM areas displaying the top 12 stacked frames of the surface for Fe (top), Cr (middle), and O (bottom).

Table 1. Order Between Grains of the Three Main Crystal Orientations for the Oxygen Layer Thickness and the Cr^+/Fe^+ Ratio for Surfaces with a Different Oxidation State.

Surface	Oxygen layer thickness	Cr^+/Fe^+ ratio
Oxidized: 450°C for 20 min	{011} > {111} > {001}	{001} > {111} > {011}
Oxidized: 300°C for 20 min	{111} > {011} and {001}	{001}, {111}, and {011}
Nonoxidized: reference	{111} > {011} and {001}	{001} and {111} > {011}

et al. (2018): the sequence in the oxidation rate of crystal planes parallel to the surface for Fe–Cr steel is {001} < {111} and {011}. The oxidation of iron is often used as a reference system, as it is a base element in many steel alloys. By itself it is already a complex system, but after comparison of its sequence of the oxidation rate with the Fe–Cr alloy in this study, it is seen that the addition of one element can drastically change the grain-dependent oxidation behavior.

The early work on the initial oxidation of Fe–Cr single crystals showed that an iron oxide outer layer that formed later on the (1 0 0) crystal is a normal or inverse spinel-type phase with fcc symmetry; however, no ordering was found on the (1 1 0) crystal (Leygraf et al., 1975). At temperatures above 200°C, the diffusion speed of cations is promoted. Fe is diffusing faster through layers on the {011} and {111}, compared to the more structured layers on the {001} oriented grains. The precise reason for the {011} overtaking the {111} is not known here and forms the key question in the future work.

Conclusions

In this work, correlative microscopy is applied on the surface of oxidized polycrystalline steel. This novel approach has been demonstrated to be successful in generating element-specific depth profiles made on selected micrometer-sized grains. Sub-micron-sized oxide spheres are formed at the surface which tend to grow in size during the oxidation of the surface in air. The nodular structure is investigated with TOF-SIMS and shown to consist of iron oxides.

The nodules are more present on grains with the {011} crystal orientation. Based on the oxide depth profile of the three grain orientations, it is confirmed that the oxidation progresses in two stages with different final oxide layer thicknesses:

- Stage 1, which includes the passive layer and an induced thermal oxide layer formed up to 300°C: {111} > {011} and {001}
- Stage 2 with thermal oxidation to 450°C: {011} > {111} > {001}.

Depth profiles of the chemical composition show that at Stage 2, the Cr^+/Fe^+ and CrO_2^-/FeO_2^- ratios are in the order {001} > {111} > {011}. At this stage, the thinnest oxide, but the highest presence of chromium and chromium oxide, is found on the {001} oriented grains. The thickest oxide is seen on the {111} oriented grain, while having the lowest presence of chromium and chromium oxide.

During the early oxidation stages observed in this work, the {001} oriented grains have shown to stimulate the highest chromium enrichment in the oxide layer and offer therefore better corrosion protection compared to the other grain orientations.

https://doi.org/10.1017/S1431927619015319 Published online by Cambridge University Press

Acknowledgments. This research was carried out under the project number T63.3.12480 in the framework of the research program of the Materials innovation institute, Delft, the Netherlands.

References

Cabrera N & Mott NF (1949). Theory of the oxidation of metals. *Rep Prog Phys* **12**, 163–184.

Constable FH (1928). Spectroscopic observations on the growth of oxide films on iron, nickel, and copper. *Proc R Soc A* **117**, 376–387.

Díaz B, Härkönen E, Światowska J, Seyeux A, Maurice V, Ritala M & Marcus P (2014). Corrosion properties of steel protected by nanometre-thick oxide coatings. *Corros Sci* **82**, 208–217.

Ekelund S & Leygraf C (1973). A LEED-AES study of the oxidation of Cr(110) and Cr(100). *Surf Sci* **40**, 179–199.

Evans UR (1925). The colours due to thin films on metals. *Proc R Soc A* **107**, 228–237.

Fujiyoshi H., Matsui T. & Yuhara J. (2012). Segregation and morphology on the surface of ferritic stainless steel (001). *Appl Surf Sci* **258**, 7664–7667.

Fushimi K, Kazuhisa A & Seo M (1999). Evaluation of heterogeneity in thickness of passive iron by scanning flectrochemical microscopy films on pure. *ISIJ Int* **39**, 346–351.

Fushimi K, Takabatake Y, Nakanishi T & Hasegawa Y (2013). Microelectrode techniques for corrosion research of iron. *Electrochim Acta* **113**, 741–747.

Gewinner G, Peruchetti JC, Jaegle A & Kalt A (1978). Photoemission study of the chromium(111) surface interacting with oxygen. *Surf Sci* **78**, 439–458.

Giannuzzi LA & Stevie FA (2005). *Introduction to Focused Ion Beams: Instrumentation, Theory, Techniques and Practice*. Springer, New York.

Grinberg Dana A, Starostin M, Shter GE, Buk A, Dinner O & Grader GS (2014). Metal corrosion screening in a nitrogen-based fuel at high temperature and pressure. *Oxid Met* **82**, 491–508.

Higginson RL, Jackson CP, Murrell EL, Exworthy PAZ, Mortimer RJ, Worrall DR & Wilcox GD (2015). Effect of thermally grown oxides on colour development of stainless steel. *Mater High Temp* **32**, 113–118.

Jin S & Atrens A (1990). Passive films on stainless steels in aqueous media. *Appl Phys A* **50**, 287–300.

Jonsson T, Karlsson S, Hooshyar H, Sattari M, Liske J, Svensson J-E & Johansson L-G (2016). Oxidation after breakdown of the chromium-rich scale on stainless steels at high temperature: Internal oxidation. *Oxid Met* **85**, 509–536.

Jonsson T, Pujilaksono B, Heidari H, Liu F, Svensson J-E, Halvarsson M & Johansson L-G (2013). Oxidation of Fe–10Cr in O_2 and in $O_2 + H_2O$ environment at 600°C: A microstructural investigation. *Corros Sci* **75**, 326–336.

Kim D-I, Hong SH, Phaniraj MP, Han HN, Ahn J-P & Cho YW (2011). Microstructural analysis of oxide layer formation in ferritic stainless steel interconnects. *Mater High Temp* **28**, 285–289.

Leygraf C, Hultquist G & Ekelund S (1975). A LEED/AES study of the oxidation of $Fe_{0.84}Cr_{0.16}$ (100) and (110). *Surf Sci* **51**, 409–432.

Lince JR, Didziulis SV, Shuh DK, Durbin TD & Yarmoff JA (1992). Interaction of O_2 with the $Fe_{0.84}Cr_{0.16}$(001) surface studied by photoelectron spectroscopy. *Surf Sci* **277**, 43–63.

Mamede AS, Nuns N, Cristol AL, Cantrel L, Souvi S, Cristol S & Paul JF (2016). Multitechnique characterisation of 304L surface states oxidised at high temperature in steam and air atmospheres. *Appl Surf Sci* **369**, 510–519.

Maurice V, Cadot S & Marcus P (2000). XPS, LEED and STM study of thin oxide films formed on Cr(110). *Surf Sci* **458**, 195–215.

Maurice V & Marcus P (2012). Passive films at the nanoscale. *Electrochim Acta* **84**, 129–138.

Michel P & Jardin C (1973). Oxygen adsorption and oxide formation on Cr (100) and Cr(110) surfaces. *Surf Sci* **36**, 478–487.

Olefjord I (1975). ESCA studies of the composition profile of low temperature oxide formed on chromium steels—I. Oxydation in dry oxygen. *Corros Sci* **15**, 687–696.

Olefjord I & Fischmeister H (1975). ESCA studies of the composition profile of low temperature oxide formed on chromium steels—II. Corrosion in oxygenated water. *Corros Sci* **15**, 697–707.

Olsson COA & Landolt D (2003). Passive films on stainless steels—Chemistry, structure and growth. *Electrochim Acta* **48**, 1093–1104.

Ossowski T & Kiejna A (2015). Oxygen adsorption on Fe(110) surface revisited. *Surf Sci* **637–638**, 35–41.

Parkinson GS (2016). Iron oxide surfaces. *Surf Sci Rep* **71**, 272–365.

Pujilaksono B, Jonsson T, Heidari H, Halvarsson M, Svensson J-E & Johansson L-G (2011). Oxidation of binary FeCr alloys (Fe–2.25Cr, Fe–10Cr, Fe–18Cr and Fe–25Cr) in O_2 and in $O_2 + H_2O$ environment at 600°C. *Oxid Met* **75**, 183–207.

Qin F, Magtoto NP, Garza M & Kelber JA (2003). Oxide film growth on Fe (111) and scanning tunneling microscopy induced high electric field stress in Fe_2O_3/Fe(111). *Thin Solid Films* **444**, 179–188.

Ramachandran D, Egoavil R, Crabbe A, Hauffman T, Abakumov A, Verbeeck J, Vandendael I, Terryn H & Schryvers D (2016). TEM and AES investigations of the natural surface nano-oxide layer of an AISI 316L stainless steel microfibre. *J Microsc* **264**, 207–214.

Rossi A, Elsener B, Hähner G, Textor M & Spencer ND (2000). XPS, AES and ToF-SIMS investigation of surface films and the role of inclusions on pitting corrosion in austenitic stainless steels. *Surf Interface Anal* **29**, 460–467.

Saeki I, Saito T, Furuichi R, Konno H, Nakamura T, Mabuchi K & Itoh M (1998). Growth process of protective oxides formed on type 304 and 430 stainless steels at 1273 K. *Corros Sci* **40**, 1295–1305.

Schreiber A, Rosenkranz C & Lohrengel MM (2007). Grain-dependent anodic dissolution of iron. *Electrochim Acta* **52**, 7738–7745.

Seyeux A, Zanna S, Allion A & Marcus P (2015). The fate of the protective oxide film on stainless steel upon early stage growth of a biofilm. *Corros Sci* **91**, 352–356.

Takabatake Y, Kitagawa Y, Nakanishi T, Hasegawa Y & Fushimi K (2016). Heterogeneity of a thermal oxide film formed on polycrystalline iron observed by two-dimensional ellipsometry. *J Electrochem Soc* **163**, C815–C822.

Takabatake Y, Kitagawa Y, Nakanishi T, Hasegawa Y & Fushimi K (2017). Grain dependency of a passive film formed on polycrystalline iron in pH 8.4 borate solution. *J Electrochem Soc* **164**, C349–C355.

Tardio S, Abel M-L, Carr RH, Castle JE & Watts JF (2015). Comparative study of the native oxide on 316L stainless steel by XPS and ToF-SIMS. *J Vac Sci Technol A* **33**, 05E122.

Vernon WHJ, Calnan EA, Clews CJB & Nurse TJ (1953). The oxidation of iron around 200°C. *Proc R Soc A* **216**, 375–397.

Vernon WHJ, Wormwell F & Nurse TJ (1939). The thickness of air-formed oxide films on iron. *J Chem Soc* 621–632.

Weiss W & Ranke W (2002). Surface chemistry and catalysis on well-defined epitaxial iron-oxide layers. *Prog Surf Sci* **70**, 1–151.

Yuan J, Wang W, Zhang H, Zhu L, Zhu S & Wang F (2016). Investigation into the failure mechanism of chromia scale thermally grown on an austenitic stainless steel in pure steam. *Corros Sci* **109**, 36–42.

Zijlstra G, de Jeer LTH, Ocelík V & De Hosson JTM (2018). The effect of surface texture on the oxidation behaviour of polycrystalline Fe-Cr. *Appl Surf Sci* **459**, 459–467.

https://doi.org/10.1017/S1431927619015319 Published online by Cambridge University Press